

# Anisotropic propagation of GHz surface and bulk acoustic waves in gallium arsenide studied by random scattering

Thomas Steenbergen, Maja Wohlfarth, Pim Veefkind, Matteo Fiscaro, and Wolfgang Löffler  
*Leiden Institute of Physics, Leiden University, P.O. Box 9504, 2300 RA Leiden, The Netherlands*

Understanding the complex anisotropic acoustic propagation in crystals is crucial for optimizing the performance of surface and bulk acoustic wave devices. Here, we investigate the anisotropy and coupling of GHz acoustic modes in (001)-cut gallium arsenide through theory and experiment. We first numerically calculate the angle-dependent phase velocities for surface and bulk modes, and we provide a code which can easily be adapted to different material systems. We validate our theoretical model experimentally by exciting surface modes with an interdigital transducer, and achieve omnidirectional acoustic propagation through random scattering of the acoustic waves. We measure the complex acoustic field with a scanning optical interferometer, and extract the angle-dependent velocities of surface and bulk modes using Fourier domain analysis. Our method could be used for the optimization of GHz-range classical and quantum acoustic devices, by studying losses of surface and bulk modes.

## I. INTRODUCTION

Anisotropic crystalline materials enable the piezoelectric excitation of high-frequency surface acoustic waves (SAWs), while simultaneously giving rise to complex, direction-dependent acoustic propagation. The small wavelength of GHz-range SAWs compared to their electromagnetic counterpart enables the miniaturization of filters in telecommunications [1, 2], while their surface confinement is widely employed in chemical [3] and biological [4] sensing applications. More recently, GHz SAWs have emerged as promising carriers of quantum information, due to their long coherence times and their ability to couple to a variety of quantum systems. These include superconducting qubits [5–7], point defects in diamond [8] and 2D materials [9], and semiconductor quantum dots hosted in gallium arsenide (GaAs) [10–12]. Understanding the complex anisotropic acoustic propagation in crystals is crucial for optimizing the performance of SAW-based (quantum) devices [13].

The anisotropic nature of acoustic propagation in GaAs stems from its zinc-blende crystal structure, which is shown in Fig. 1(a). The mechanical polarization of SAWs generally consists of three components, but in high-symmetry directions [100] and [110], only the longitudinal and vertical transverse components remain, as illustrated in Fig. 1(b). The SAW displacements decay exponentially into the material, as shown in Fig. 1(c). The electromechanical coupling in (001) cut GaAs is relatively weak ( $\kappa^2 = 0.07\%$  [14]), but is essential for the electrical excitation of acoustic waves using interdigital transducers (IDTs). As the coupling vanishes along the [100] axis and is maximal along the [110] direction, electrical excitation is often performed along the [110] direction.

Calculating the angle-dependent velocities of surface modes in piezoelectric materials is nontrivial, as it requires solving the piezo-elastic wave equations while enforcing surface boundary conditions. Several theoretical approaches have been developed for this purpose.

The Stroh formalism [15], which is used here, offers a matrix-based framework in which boundary conditions are easily enforced. Partial-wave methods [16] offer a more intuitive formulation [17] and are readily extended to layered structures, while Green’s function approaches provide time-domain waveforms, energy flux, and group velocities [18, 19]. Given the complexity of such calculations, we include ready-to-run code [20] to facilitate calculations for a variety of crystalline materials.

Measurements of the angle-dependent SAW phase velocity in GaAs have been reported using Brillouin spectroscopy [21] and by varying the orientation of IDTs [22], while group velocities have been measured using an optical pump–probe technique based on laser-generated SAW pulses [19]. Bulk acoustic wave (BAW) velocities have been measured along high-symmetry directions [100] and [110] [23, 24], but full angle-dependent measurements have not been reported to date.

In this work, we first numerically calculate the angle-dependent velocities of surface and bulk acoustic waves in GaAs. We compare the theoretical results with experimental measurements, where SAWs are generated using an IDT and omnidirectional propagation is obtained by randomly distributed scattering centers. The out-of-plane amplitude and phase of the acoustic field are mapped using a scanning optical interferometer [25], and the angle-dependent velocities are extracted using complex Fourier analysis [26]. Since the presented measurement technique allows for the simultaneous measurement of surface and bulk modes, it can be used to optimize acoustic devices by identifying loss mechanisms.

## II. ACOUSTIC WAVE THEORY

The coupled equations that need to be solved to find the different modes of acoustic propagation in piezoelectric solids combine Hooke’s law and Newton’s second law with piezoelectric coupling [14]:

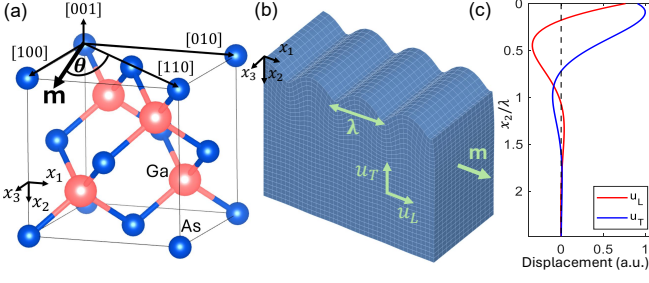


FIG. 1. Crystal structure and surface wave displacement. GaAs crystal structure (a), where the coordinate system  $(x_1, x_2, x_3)$  is aligned with the crystallographic directions. Sketch of a SAW propagating in the  $[100]$  direction (b), where the surface is defined by the  $(x_1, x_3)$  plane. Depth-dependent longitudinal ( $u_L$ ) and transverse ( $u_T$ ) displacements (c) for the same SAW mode.

$$c_{ijkl} \frac{\partial^2 u_l}{\partial x_j \partial x_k} + e_{kij} \frac{\partial^2 \Phi}{\partial x_k \partial x_j} = \rho \frac{\partial^2 u_i}{\partial t^2}, \quad (1a)$$

$$-\epsilon_{ijk} \frac{\partial^2 \Phi}{\partial x_j \partial x_k} + e_{jkl} \frac{\partial^2 u_l}{\partial x_j \partial x_k} = 0, \quad (1b)$$

where  $i, j, k, l = 1, 2, 3$  and  $c_{ijkl}$  is the elastic stiffness tensor,  $u_l$  the mechanical displacement,  $e_{ijk}$  the piezoelectric tensor,  $\Phi$  the electrical potential,  $\rho$  the mass density and  $\epsilon_{ij}$  the dielectric tensor. The Cartesian coordinate system  $(x_1, x_2, x_3)$  is aligned with the crystal axes of GaAs as shown in Fig. 1(a). All material tensors and properties of GaAs are provided in Appendix A.

To find bulk wave solutions, we assume the medium to be infinite in all dimensions, allowing plane wave solutions without boundary conditions. We use the following combined plane wave ansatz for  $\mathbf{u}$  and  $\Phi$ :

$$\begin{bmatrix} \mathbf{u}(\mathbf{x}, t) \\ \Phi(\mathbf{x}, t) \end{bmatrix} = \mathbf{a} \exp \left[ ik(\mathbf{m} \cdot \mathbf{x} - vt) \right], \quad (2)$$

where  $k$  is the wave number,  $\mathbf{m}$  the propagation direction vector,  $v$  the phase velocity and  $\mathbf{a} = [\mathbf{a}_m, a_\Phi]^T$  is the 4D state vector containing the mechanical displacement vector  $\mathbf{a}_m$  and the electric potential  $a_\Phi$ . After substituting the plane-wave ansatz (Eq. (2)) into Eqs. (1a,b) and eliminating the potential  $\Phi$ , we obtain the Christoffel eigenvalue equation [14]:

$$\tilde{\Gamma} \mathbf{a}_m = \rho v^2 \mathbf{a}_m, \quad (3)$$

where  $\tilde{\Gamma}$  is the  $3 \times 3$  piezoelectric Christoffel matrix, which is constructed from  $c_{ijkl}$ ,  $e_{ijk}$ ,  $\epsilon_{jk}$  and the propagation direction  $\mathbf{m}$  (see Appendix B). Finding the different modes of propagation and their phase velocities now reduces to solving the eigenvalue problem (Eq. 3), where the eigenvectors  $\mathbf{a}_m$  describe the mechanical displacement, and the eigenvalues  $\rho v^2$  determine

the corresponding phase velocities. To obtain angle-dependent velocities, we define the propagation vector  $\mathbf{m} = (\cos(\frac{\pi}{4} - \theta), 0, \sin(\frac{\pi}{4} - \theta))$  and determine the solutions for the in-plane angle  $\theta$ , see Fig. 1(a). We find 3 modes: a (quasi-) longitudinal mode (L-BAW), a (quasi-) horizontal shear mode (SH-BAW) and a vertical shear mode (SV-BAW). In general, the L-BAW and SH-BAW are coupled and therefore referred to as quasi-modes, but along the  $[100]$  and  $[110]$  directions they decouple into pure polarizations. Sketches of the mechanical displacements of these bulk modes propagating along the  $[100]$  direction are shown in Fig. 2(a-c).

Now, to construct surface modes, we first define a half-space where the material surface is spanned by the  $(x_1, x_3)$  plane, with inward surface normal  $\mathbf{n} = (0, 1, 0)$  [see Fig. 1(b)]. We assume a stress-free, electrically open-circuited material surface and search for surface-bound solutions of the form [27]:

$$\mathbf{U}_n = \begin{bmatrix} \mathbf{u}(\mathbf{x}, t) \\ \Phi(\mathbf{x}, t) \end{bmatrix} = \mathbf{a}_n \exp \left[ ik(\mathbf{m} \cdot \mathbf{x} + p_n \mathbf{n} \cdot \mathbf{x} - vt) \right], \quad (4)$$

which represents a partial surface wave (with  $\mathbf{a}$ ,  $k$ ,  $\mathbf{m}$ ,  $v$  defined as above), with an additional complex decay parameter  $p$ , indicating the decay into the substrate along  $\mathbf{n}$ . A surface mode then,  $\mathbf{U}_{SM}$ , consists of a linear combination of 4 partial waves [27]:

$$\mathbf{U}_{SM} = \sum_{n=1}^4 B_n \mathbf{U}_n, \quad (5)$$

where  $B_n$  are complex coefficients representing the relative weights of the partial waves to the surface mode.

To determine the four partial wave solutions  $\mathbf{U}_n$  and to impose the boundary conditions for a range of propagation angles and velocities, we employ the dynamic elastic Stroh formalism [27], extended to piezoelectric media [28, 29]. The Stroh formalism reformulates the coupled wave equations (Eqs. 1(a,b)) together with the ansatz (Eq. 4) into an 8-dimensional eigenvalue problem:

$$\mathbf{N} \begin{bmatrix} \mathbf{a} \\ \mathbf{l} \end{bmatrix} = p \begin{bmatrix} \mathbf{a} \\ \mathbf{l} \end{bmatrix}, \quad (6)$$

where  $\mathbf{N}$  is the  $8 \times 8$  Stroh matrix, constructed from  $c_{ijkl}$ ,  $e_{ijk}$ ,  $\epsilon_{jk}$ , the trial velocity  $v$  and the propagation direction  $\mathbf{m}$ , see Appendix C for its exact construction. The Stroh eigenvector  $[\mathbf{a}, \mathbf{l}]^T$  contains besides the state vector  $\mathbf{a}$  the generalized traction vector  $\mathbf{l} = [\boldsymbol{\sigma}, D]^T$ , which includes the stress vector  $\boldsymbol{\sigma}$  and the electric displacement  $D$  of the partial wave at the surface. The eigenvalues of Stroh matrix,  $p$ , come in conjugate pairs. In the following, we outline the procedure for obtaining the four partial waves  $\mathbf{U}_n$ , and how the angle-dependent velocity and coefficients  $B_n$  can be obtained by imposing boundary conditions. A flowchart of this procedure is provided in Appendix D.

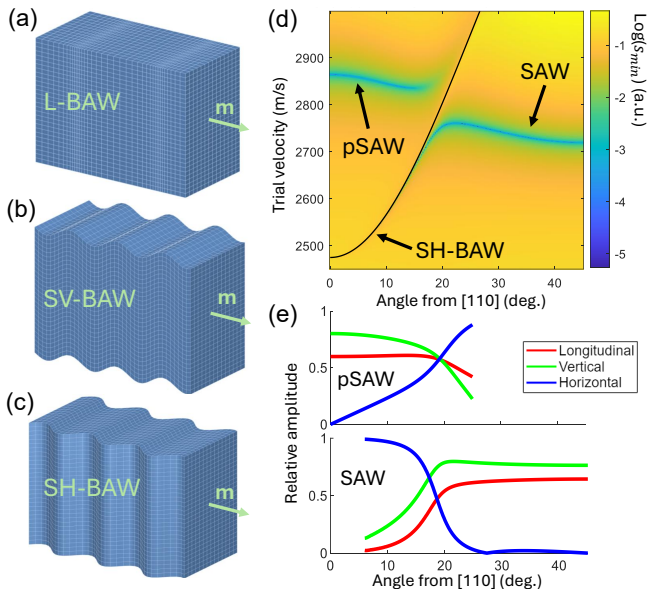


FIG. 2. BAW displacements and surface mode velocities and polarization. Sketches (a-c) of the mechanical displacement of the three BAW modes, propagating in the [100] direction. Theoretical boundary condition fulfillment (d),  $s_{\min}$ , of the four chosen partial waves from the Stroh formalism, plotted on a logarithmic scale between the [110] and [100] crystal axes. Relative angle-dependent amplitudes (e) of the mechanical polarizations of the SAW and pSAW modes.

We first construct the Stroh matrix for a range of propagation angles and trial velocities. By calculating its eigenvectors  $\mathbf{a}$  and corresponding eigenvalues  $p$ , we obtain 8 partial wave solutions in the form of Eq. (4). To identify surface-bound modes, we select the four partial waves with the highest positive imaginary parts of  $p$ ,  $\Im(p)$ , corresponding to waves that decay into the substrate. Depending on the propagation angle and the trial velocity, we find either 4 partial waves with  $\Im(p) > 0$  or only three partial waves with  $\Im(p) > 0$  (the other partial wave having  $\Im(p) = 0$ ). We thus find a mode strongly confined to the surface, the *pure* surface acoustic wave (SAW), and a mode that is more weakly confined to the surface, of which one partial wave does not decay with depth, the *pseudo* surface acoustic wave (pSAW).

Once the partial waves  $\mathbf{U}_n$  have been obtained for each propagation angle and trial velocity, we must now determine the velocity for which the boundary conditions can be satisfied by an appropriate choice of coefficients  $B_n$ . The boundary information of the four selected partial waves is contained in their generalized traction vectors  $\mathbf{l}_n$ , from which we construct the  $4 \times 4$  traction matrix  $\mathbf{L} = [\mathbf{l}_1, \mathbf{l}_2, \mathbf{l}_3, \mathbf{l}_4]$  [27]. Stress-free and open-circuited boundary conditions ( $\sigma_i = 0, D = 0$ ) are satisfied if there exists a vector of coefficients  $\mathbf{B} = [B_1, B_2, B_3, B_4]^T$  ( $B_n$  in Eq. (5)), such that:

$$\mathbf{L}\mathbf{B} = 0, \quad (7)$$

which is the case if  $\det(\mathbf{L}) = 0$  [27]. We evaluate this numerically using a singular value decomposition (SVD) of the traction matrix  $\mathbf{L}$ . If the smallest singular value  $s_{\min}$  vanishes, then there is a combination of coefficients  $B_n$ , such that surface mode  $U_{SM}$  satisfies the boundary conditions.

We plot  $s_{\min}$  for a range of angles and velocities in Fig. 2(d). We observe two branches where  $s_{\min}$  is minimized and where the boundary conditions are thus fulfilled. These branches represent the angle-dependent phase velocities of the SAW mode and the pSAW mode. For these modes, the coefficients  $B_n$  are obtained from the right singular vector corresponding to  $s_{\min}$ . Together with the four selected eigenvalues  $p_n$  and eigenvectors  $\mathbf{a}_n$ , we now have constructed for both modes the complete depth-dependent mechanical polarization and electrical potential  $U_{SM}$  for every propagation angle. We plot the angle-dependent amplitude of the mechanical polarization at the surface for the pseudo mode (pSAW, upper figure) and the pure mode (SAW, lower figure) in Fig. 2(e). Here we find that the mechanical polarization generally comprises three components. Along [110] for the pSAW and along [100] and  $27^\circ$  from [110] for the SAW, the mechanical polarization consists of only vertical and longitudinal components.

We observe in Fig. 2(d) that the surface modes (pSAW and SAW) exhibit an avoided crossing with the SH-BAW mode, suggesting a coupling of the surface and bulk modes for angles around  $18^\circ$  from the [110] axis. Approaching the anti-crossing, we find that the surface modes acquire a strong horizontal component (Fig. 2(e)), which is the main polarization of the SH-BAW. This suggests that coupling between surface and bulk modes can indeed explain the anti-crossing. Finally, we would like to point out that exactly in the [110] direction, the non-decaying partial wave of the pseudo mode vanishes due to the crystal symmetry. Hence, precisely along [110], the pSAW mode is non-leaky [19].

### III. EXPERIMENTAL SETUP

In the experiment, we generate surface modes with an IDT and omnidirectional propagation is achieved by randomly positioned scattering centers, see Fig. 3. The IDT and the disk-shaped scattering centers (diameter  $1.4 \mu\text{m}$ ) are fabricated on a (001)-cut GaAs substrate using an electron-beam lithography lift-off process and consist of a 5 nm titanium adhesion layer, a 40 nm aluminum layer and a 5 nm titanium capping layer. The IDT has 50 finger pairs and the fingers are 700 nm wide and  $312 \mu\text{m}$  long. The periodicity of the IDT fingers is chosen at  $2.8 \mu\text{m}$  [see inset Fig. 3(b)], to efficiently generate surface modes at 1.032 GHz ( $v_{pSAW} \approx 2860 \text{ m/s}$  in the [110] direction).

The out-of-plane acoustic displacement is measured with an optical scanning Michelson interferometer [25], in which laser light is focused on the acoustic scattering

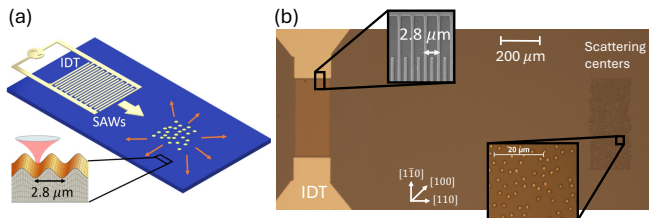


FIG. 3. Experimental setup. Schematic (a) of the acoustic scattering sample, where the inset depicts the optical measurement of the acoustic field. Optical microscope image (b) of the acoustic scattering device, with inset showing a scanning electron microscope image of the IDT finger structure.

sample with a spot size of around  $3 \mu\text{m}$  [see inset Fig. 3(a)]. The optical path length is modified by the out-of-plane component of the acoustic displacement, which leads to a GHz modulation of the interferometric signal that is read-out using a lock-in technique, allowing for the extraction of the amplitude and phase of the acoustic displacement. To obtain high-resolution spatial scans, the acoustic sample is mounted on a motorized XYZ translation stage with a step size of  $14 \text{ nm}$  in the  $x$  direction (the  $[110]$  crystal axis) and  $1 \mu\text{m}$  in the  $y$  direction (the  $[\bar{1}\bar{1}0]$  crystal axis).

#### IV. RESULTS AND DISCUSSION

We show the measurements of the amplitude and phase of the demodulated interferometric signal in Fig. 4(a) and (b), respectively, where the measured area is indicated by the dashed black box in Fig. 4(d). In the amplitude measurement, we observe a beam of surface modes generated by the IDT directed towards the scattering area, which is indicated by the dashed white box (a.i). A significant portion of the acoustic field, however, is not affected by the scattering area (around 80%). Nevertheless, as we will show later, the scattered waves provide sufficient signal to extract the angle-dependent velocities of the acoustic modes in all directions. We also observe rays propagating in a variety of directions (a.ii) from the scattering area, which are due to random-wave interference. In the phase measurement, we observe again the incoming beam, now with a periodic sawtooth pattern between  $-\pi$  and  $+\pi$  with the expected periodicity of the pSAW wavelength of around  $2.8 \mu\text{m}$ , as shown in the inset.

To distinguish the different acoustic modes by their angle-dependent wavelengths, we perform spatial Fourier analysis. For this, we first combine the amplitude and phase measurements of the area depicted by the dashed red box in Fig. 4(d) in a complex field, of which we take the spatial 2D fast Fourier transform (FFT). We choose this area to exclude the field in the scattering area, as its random spatial periodicities result in noise and artefacts in the spatial FFT. We select only the back-scattered field

(i.e. waves moving to the left in Fig. 4(a,b)), which corresponds to spatial frequencies  $\nu_x > 0$ . Next, we fold the remaining spatial Fourier data twice by averaging: first across the  $[110]$  axis, and then across the diagonal  $[100]$  axis. This folding reduces the  $180^\circ$  range of propagation directions to a  $45^\circ$  sector.

In Fig. 4(c), we plot the magnitude of the folded FFT between the  $[110]$  and the  $[100]$  crystal axes. In this figure, we identify acoustic modes by their angle-dependent spatial periodicity  $(\nu_x, \nu_y)$ . We find a strong signal associated with the pure SAW mode at the  $[100]$  axis, which does not fully extend to the  $[110]$  axis, but exhibits an avoided crossing with the pSAW mode, which then extends to the  $[110]$  axis. This observation is in line with the theoretical results (see Fig. 2(d)). We also observe a clear signal corresponding to the L-BAW and a weaker signal associated with the SH-BAW. We further observe two sidebands (indicated by \*) of the surface modes. Since they are equally spaced from the main signal in the  $\nu_x$  direction and decrease in amplitude for higher  $\nu_x$ , we hypothesize that these sidebands are the result of an amplitude modulation in the  $x$  direction caused by imperfections of the translation stage [30].

Finally, we calculate for each acoustic mode the weighted averages  $(\bar{\nu}_x, \bar{\nu}_y)$  for a set of angles, which are depicted as red dots in Fig. 4(c). This is achieved using a combined ridge detection and clustering algorithm, which robustly identifies the data points that correspond to a mode. We calculate the average of these selected data points within an angular bin with the FFT amplitude as weight, and we obtain  $(\bar{\nu}_x, \bar{\nu}_y)$ . We then calculate the propagation angle  $\theta$  (from the  $[110]$  axis) and the corresponding phase velocity  $v(\theta)$  as follows:

$$\theta = \arctan\left(\frac{\bar{\nu}_y}{\bar{\nu}_x}\right), \quad (8)$$

$$v(\theta) = \frac{f}{\sqrt{\bar{\nu}_x^2 + \bar{\nu}_y^2}}, \quad (9)$$

where the  $f$  is the excitation frequency of  $1.03205 \text{ GHz}$ . The resulting angle-dependent velocities are shown in Fig. 4(e), where the dots are the experimental data and the curves are the theoretical predictions. We find a very good agreement between experiment and theory.

At first glance, the measurement of BAW modes is surprising, as they lack an out-of-plane displacement component (see Fig. 2(a,c)) and therefore should not modulate the optical path length – the principle underlying our detection technique. However, stress-free boundary conditions alter the displacement profile of the modes near the surface, possibly introducing an out-of-plane component. In addition, a modulation of the refractive index by the acousto-optic effect [31, 32] could contribute to the measured signal. Interestingly, despite exhibiting an out-of-plane displacement component, the SV-BAW is not observed and the origin of its absence remains unclear.

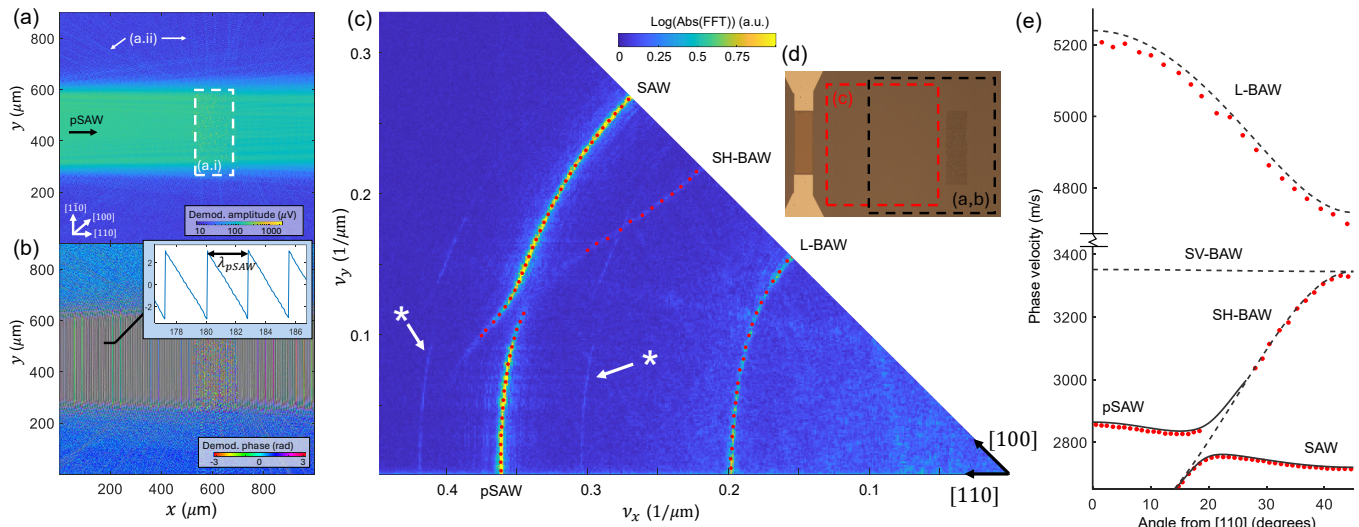


FIG. 4. Experimental results and comparison to theory. Rms amplitude (a, logarithmic scale) and phase (b) of the 1.03205 GHz demodulated interferometric signal, measured on the area indicated by the black dashed box in the microscope image (d). Absolute value (c) of the spatial Fourier transform of the complex measurement of the area indicated by the red dashed box in (d). The data is folded to a 45 degree sector and the values  $(\bar{v}_x, \bar{v}_y)$  are shown in red. Comparison (e) between the measured (red dots) and theoretical angle-dependent velocities of the surface (black curves) and bulk (dashed black curves) acoustic modes.

## V. CONCLUSION AND OUTLOOK

In conclusion, we measured the angle-dependent velocity of surface and bulk acoustic waves in (001) cut GaAs and we found excellent agreement with theoretical calculations. For our calculations, we employed the piezoelectric Christoffel formalism for bulk modes and the extended Stroh formalism for surface modes, and our published code can easily be extended to different material systems. In the experiment, we generated acoustic waves using an IDT, and omnidirectional propagation is obtained by randomly positioned scattering centers. The out-of-plane acoustic displacement is mapped with a scanning optical interferometer and using complex Fourier analysis, the angular dispersion of surface and bulk modes was obtained. Interestingly, bulk modes, which in the bulk have no out-of-plane displacement, were measured at the surface. This measurement technique, combined with Fourier analysis, could be used for the optimization of (quantum) acoustic devices by studying bulk loss mechanisms. The acoustic scattering device can furthermore be employed to investigate acoustic wave propagation in random media [33–35].

## ACKNOWLEDGMENTS

We thank Harry Visser and Peter van Veldhuizen for their help with RF electronics. We acknowledge funding from NWO (680.92.18.04), NWO/OCW (Quantum Software Consortium Nos. 024.003.037 and 024.003.037/3368, Quantum Limits No. SUM-

MIT.1.1016), and from the Dutch Ministry of Economic Affairs (Quantum Delta NL).

## DATA AVAILABILITY

The theoretical model and data is online available [20]. The experimental data underlying the results presented in this paper can be obtained from the authors upon reasonable request.

## APPENDIX A: GAAS MATERIAL PROPERTIES

We provide here the material properties of GaAs. The fourth-rank stiffness tensor  $c_{ijkl}$  is represented in contracted Voigt notation as the  $6 \times 6$  matrix  $c_{\alpha\beta}$  and the third-rank piezoelectric tensor  $e_{ijk}$  as the  $3 \times 6$  matrix  $e_{i\alpha}$ . The tensor indices are mapped to matrix indices according to:

$$\begin{aligned}
 (ij, kl) &\rightarrow (\alpha, \beta) \\
 (11) &\rightarrow 1 \\
 (22) &\rightarrow 2 \\
 (33) &\rightarrow 3 \\
 (23), (32) &\rightarrow 4 \\
 (13), (31) &\rightarrow 5 \\
 (12), (21) &\rightarrow 6
 \end{aligned}$$

The elastic tensor for GaAs is given by:

$$\mathbf{c}_{\alpha\beta} = \begin{bmatrix} c_{11} & c_{12} & c_{12} & 0 & 0 & 0 \\ c_{12} & c_{11} & c_{12} & 0 & 0 & 0 \\ c_{12} & c_{12} & c_{11} & 0 & 0 & 0 \\ 0 & 0 & 0 & c_{44} & 0 & 0 \\ 0 & 0 & 0 & 0 & c_{44} & 0 \\ 0 & 0 & 0 & 0 & 0 & c_{44} \end{bmatrix}, \quad (\text{A.1})$$

with [14]:

$$c_{11} = 118.8 \text{ GPa}, \quad c_{12} = 53.8 \text{ GPa}, \quad c_{44} = 59.4 \text{ GPa}.$$

The piezoelectric tensor is given by:

$$\mathbf{e}_{i\alpha} = \begin{bmatrix} 0 & 0 & 0 & e_{14} & 0 & 0 \\ 0 & 0 & 0 & 0 & e_{14} & 0 \\ 0 & 0 & 0 & 0 & 0 & e_{14} \end{bmatrix}, \quad (\text{A.2})$$

with [14]:

$$e_{14} = -0.16 \text{ C/m}^2.$$

The dielectric tensor of GaAs is given by:

$$\boldsymbol{\epsilon}_{ij} = \epsilon_s \begin{bmatrix} 1 & 0 & 0 \\ 0 & 1 & 0 \\ 0 & 0 & 1 \end{bmatrix}, \quad (\text{A.3})$$

with [14]:

$$\epsilon_s = 12.9 \epsilon_0, \quad \epsilon_0 = 8.854 \times 10^{-12} \text{ F/m}.$$

Finally, the mass density of GaAs is given by  $\rho = 5307 \text{ kg m}^{-3}$  [14].

## APPENDIX B: CHRISTOFFEL MATRIX FOR PIEZOELECTRIC SOLIDS

Here we show the construction of the  $3 \times 3$  Christoffel matrix  $\tilde{\Gamma}_{il}$  from the propagation vector  $\mathbf{m} = (m_1, m_2, m_3)$  and the material tensors. The piezoelectric Christoffel matrix is given by [14]:

$$\tilde{\Gamma}_{il} = \Gamma_{il} + \frac{\gamma_i \gamma_l}{\epsilon}, \quad (\text{A.4})$$

where:

$$\Gamma_{il} = c_{ijkl} m_j m_k, \quad (\text{A.5a})$$

$$\gamma_i = e_{kij} m_j m_k, \quad (\text{A.5b})$$

$$\epsilon = \epsilon_{jk} m_j m_k, \quad i, j, k, l = 1, 2, 3. \quad (\text{A.5c})$$

## APPENDIX C: STROH MATRIX FOR PIEZOELECTRIC SOLIDS

In this Appendix, we outline the construction of the Stroh matrix for anisotropic piezoelectric solids. We extend the dynamic  $6 \times 6$  Stroh matrix for elastic solids [27] to piezoelectric materials by incorporating piezoelectric terms in an *effective* stiffness tensor  $\tilde{C}_{ijkl}$  [28, 29], resulting in an  $8 \times 8$  Stroh matrix:

$$\mathbf{N} = \begin{bmatrix} \mathbf{N}_1 & \mathbf{N}_2 \\ \mathbf{N}_3 & \mathbf{N}_4 \end{bmatrix}, \quad (\text{A.6})$$

where the  $4 \times 4$  sub-blocks are given by:

$$\begin{aligned} \mathbf{N}_1 &= -\mathbf{T}^{-1} \mathbf{R}^T, \\ \mathbf{N}_2 &= \mathbf{T}^{-1}, \\ \mathbf{N}_3 &= \mathbf{R} \mathbf{T}^{-1} \mathbf{R}^T - \mathbf{Q}, \\ \mathbf{N}_4 &= -\mathbf{R} \mathbf{T}^{-1}. \end{aligned} \quad (\text{A.7})$$

The matrices  $\mathbf{Q}$ ,  $\mathbf{R}$ ,  $\mathbf{T}$  are defined in terms of  $\tilde{C}_{ijkl}$  as [27]

$$\begin{aligned} Q_{ik} &= \tilde{C}_{ijkl} m_j m_l, \\ R_{ik} &= \tilde{C}_{ijkl} m_j n_l, \quad j, l = 1, 2, 3, \\ T_{ik} &= \tilde{C}_{ijkl} n_j n_l, \quad i, k = 1, 2, 3, 4. \end{aligned} \quad (\text{A.8})$$

Up until now, we have constructed the static extended Stroh matrix. We obtain the dynamic Stroh matrix by including a trial velocity  $v$  in the first 3 diagonal elements of  $Q_{ik}$  [27]:

$$Q_{ik} = Q_{ik} - \rho v^2 \delta_{ik} \quad (i, k = 1, 2, 3), \quad (\text{A.9})$$

where  $\rho$  is the mass density of GaAs. The effective tensor  $\tilde{C}_{ijkl}$  is obtained by extending the conventional elastic stiffness tensor to include piezoelectric and dielectric couplings [29]:

$$\begin{aligned} \tilde{C}_{ijkl} &= c_{ijkl}, \\ \tilde{C}_{ij4l} &= e_{lij}, \\ \tilde{C}_{4jkl} &= e_{jkl}, \\ \tilde{C}_{4j4l} &= -\epsilon_{jl}, \quad i, j, k, l = 1, 2, 3. \end{aligned} \quad (\text{A.10})$$

## APPENDIX D: FLOWCHART OF SURFACE MODE CALCULATIONS

Below we provide a flowchart visualizing the algorithm used for the construction of SAW and pSAW modes and the calculation of their angle-dependent velocities.

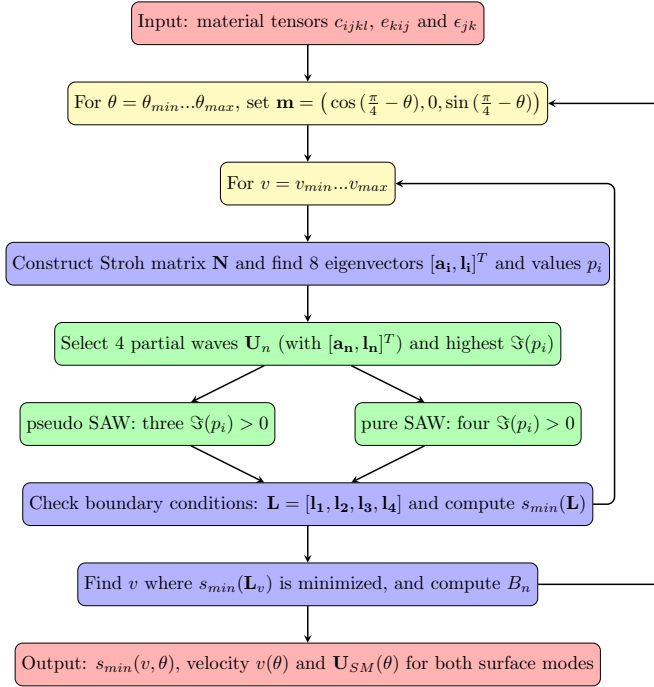


FIG. 5. Flowchart of the numerical procedure used to construct SAW and pSAW modes and to determine their angle-dependent velocities.

- 
- [1] H. A. Ali, M. I. Ibrahim, H. M. Abdelkader, and M. M. Elsherbini, High-precision saw bandpass filtering at 1747.5 mhz for lte applications using wavelet transform techniques, *Scientific Reports* **15**, 41823 (2025).
  - [2] P. Liu, S. Fu, B. Xiao, X. Zhou, Q. Xu, J. Gao, S. Zhang, R. Wang, C. Song, F. Zeng, W. Wang, and F. Pan, Scaling llsaw filters on engineered linbo3-on-sic wafer for 5g and wi-fi 6 wideband applications, *Microsystems and Nanoengineering* **11**, 148 (2025).
  - [3] X. Li, W. Sun, W. Fu, H. Lv, X. Zu, Y. Guo, D. Gibson, and Y. Q. Fu, Advances in sensing mechanisms and micro/nanostructured sensing layers for surface acoustic wave-based gas sensors, *Journal of Materials Chemistry A* **11**, 9216 (2023).
  - [4] Y. Zeng, R. Yuan, H. Fu, Z. Xu, and S. Wei, Foodborne pathogen detection using surface acoustic wave biosensors: a review, *RSC Advances* **14**, 37087 (2024).
  - [5] M. V. Gustafsson, T. Aref, A. F. Kockum, M. K. Ekström, G. Johansson, and P. Delsing, Propagating phonons coupled to an artificial atom, *Science* **346**, 207 (2014).
  - [6] R. Manenti, A. F. Kockum, A. Patterson, T. Behrle, J. Rahamim, G. Tancredi, F. Nori, and P. J. Leek, Circuit quantum acoustodynamics with surface acoustic waves, *Nature Communications* **8**, 975 (2017).
  - [7] B. A. Moores, L. R. Sletten, J. J. Viennot, and K. W. Lehnert, Cavity quantum acoustic device in the multi-mode strong coupling regime, *Physical Review Letters* **120**, 227701 (2018).
  - [8] D. A. Golter, T. Oo, M. Amezcua, I. Lekavicius, K. A. Stewart, and H. Wang, Coupling a surface acoustic wave to an electron spin in diamond via a dark state, *Physical Review X* **6**, 041060 (2016).
  - [9] S. D. Patel, K. Parto, M. Choquer, N. Lewis, S. Umezawa, L. Hellman, D. Polishchuk, and G. Moody, Surface acoustic wave cavity optomechanics with atomically thin h-bn and wse2 single-photon emitters, *PRX Quantum* **5**, 010330 (2024).
  - [10] M. Weiß and H. J. Krenner, Interfacing quantum emitters with propagating surface acoustic waves, *Journal of Physics D: Applied Physics* **51**, 373001 (2018).

- [11] R. A. Decrescent, Z. Wang, P. Imany, R. C. Boutelle, C. A. McDonald, T. Autry, J. D. Teufel, S. W. Nam, R. P. Mirin, and K. L. Silverman, Large single-phonon optomechanical coupling between quantum dots and tightly confined surface acoustic waves in the quantum regime, *Physical Review Applied* **18**, 034067 (2022).
- [12] R. A. DeCrescent, Z. Wang, J. T. Bush, P. Imany, A. Kwiatkowski, D. V. Reddy, S. W. Nam, R. P. Mirin, and K. L. Silverman, Coherent dynamics in an optical quantum dot with phonons and photons, *Optica* **11**, 1526 (2024).
- [13] M. E. Msall and P. V. Santos, Focusing surface-acoustic-wave microcavities on gaas, *Physical Review Applied* **13**, 014037 (2020).
- [14] D. Royer and E. Dieulesaint, *Elastic Waves in Solids I: Free and Guided Propagation*, 1st ed. (Springer Berlin, 1996).
- [15] A. N. Stroh, Steady state problems in anisotropic elasticity, *Journal of Mathematics and Physics* **41**, 77 (1962).
- [16] L. P. Solie and B. A. Auld, Elastic waves in free anisotropic plates, *The Journal of the Acoustical Society of America* **54**, 50 (1973).
- [17] C. Hakoda and C. J. Lissenden, Using the partial wave method for wave structure calculation and the conceptual interpretation of elastodynamic guided waves, *Applied Sciences* **8**, 966 (2018).
- [18] A. G. Every, K. Y. Kim, and A. A. Maznev, The elastodynamic response of a semi-infinite anisotropic solid to sudden surface loading, *The Journal of the Acoustical Society of America* **102**, 1346 (1997).
- [19] A. A. Maznev, A. M. Lomonosov, P. Hess, and A. A. Kolomenskii, Anisotropic effects in surface acoustic wave propagation from a point source in a crystal, *European Physical Journal B* **35**, 429 (2003).
- [20] T. A. Steenbergen and W. Löffler, *Theoretical calculations of surface and bulk acoustic waves in piezoelectric materials* (Zenodo, 2026).
- [21] M. H. Kuok, S. C. Ng, and V. L. Zhang, Angular dispersion of surface acoustic waves on (001), (110), and (111) gaas, *Journal of Applied Physics* **89**, 7899 (2001).
- [22] M. Powlowski, F. Sfigakis, and N. Y. Kim, Temperature dependent angular dispersions of surface acoustic waves on gaas, *Japanese Journal of Applied Physics* **58**, 030907 (2019).
- [23] T. B. Bateman, H. J. McSkimin, and J. M. Whelan, Elastic moduli of single-crystal gallium arsenide, *Journal of Applied Physics* **30**, 544 (1959).
- [24] M. H. Kuok, S. C. Ng, V. L. Zhang, and D. J. Lockwood, Acoustic mode dispersion at hypersonic frequencies in gaas, *Solid State Communications* **116**, 27 (2000).
- [25] M. Fiscaro, T. A. Steenbergen, Y. C. Doedes, K. Heeck, and W. Löffler, Imaging transverse modes in a ghz surface acoustic wave cavity, *Phys. Rev. Applied* **23**, 014032 (2025).
- [26] T. A. Steenbergen, M. Fiscaro, K. Czerniak, M. Rog, K. Lahabi, and W. Löffler, Young's double-slit experiment with anisotropic ghz surface acoustic waves on gallium arsenide, *Optics Letters* **50**, 6385 (2025).
- [27] K. Tanuma, Stroh formalism and rayleigh waves, *Journal of Elasticity* **89**, 5 (2007).
- [28] C. Hwu, Some explicit expressions of extended stroh formalism for two-dimensional piezoelectric anisotropic elasticity, *International Journal of Solids and Structures* **45**, 4460 (2008).
- [29] C. Hwu and W. Becker, Stroh formalism for various types of materials and deformations, *Journal of Mechanics* **38**, 433 (2022).
- [30] We investigated this effect by rotating the sample and found that the sidebands remained dominant along the same axis of the translation stage.
- [31] K. Chaudhary, M. Illienko, T. van den Hooven, S. Witte, and P. C. Planken, Optically enhancing and controlling photoacoustic signals using ultra-thin semiconductor coatings on metal surfaces, *Optics Express* **33**, 199 (2025).
- [32] P. Debye and F. W. Sears, On the scattering of light by supersonic waves, *Proc. Natl. Acad. Sci. U.S.A.* **18**, 409 (1932).
- [33] D. S. Wiersma, P. Bartolini, A. Lagendijk, and R. Righini, Localization of light in a disordered medium, *Nature* **390**, 671 (1997).
- [34] I. M. Vellekoop and A. P. Mosk, Focusing coherent light through opaque strongly scattering media, *Optics Letters* **32**, 2309 (2007).
- [35] H. Hu, A. Strybulevych, J. H. Page, S. E. Skipetrov, and B. A. V. Tiggelen, Localization of ultrasound in a three-dimensional elastic network, *Nature Physics* **4**, 945 (2008).